

Article

Visible-Light Driven Photocatalytic Degradation of Pirimicarb by Pt-Doped AgInS₂ Nanoparticles

Hweiyen Tsai ^{1,2}, Janah Shaya ^{3,4} , Siriluck Tesana ⁵, Vladimir B. Golovko ⁵,
Syuan-Yun Wang ^{1,2}, Yi-Yen Liao ^{1,2} , Chung-Shin Lu ^{6,*} and Chiing-Chang Chen ^{7,*} 

¹ Department of Medical Applied Chemistry, Chung Shan Medical University, Taichung 402, Taiwan; annetsai@csmu.edu.tw (H.T.); cindy20122224@gmail.com (S.-Y.W.); s0564023@gm.csmu.edu.tw (Y.-Y.L.)

² Department of Medical Education, Chung Shan Medical University Hospital, Taichung 402, Taiwan

³ College of Medicine and Health Sciences, Khalifa University, Abu Dhabi P.O. Box 127788, UAE; shaya.janah@ku.ac.ae

⁴ College of Arts and Sciences, Khalifa University, Abu Dhabi P.O. Box 127788, UAE

⁵ The MacDiarmid Institute for Advanced Materials and Nanotechnology, School of Physical and Chemical Sciences, University of Canterbury, Christchurch 8140, New Zealand;

siriluck.tesana@pg.canterbury.ac.nz (S.T.); vladimir.golovko@canterbury.ac.nz (V.B.G.)

⁶ Department of General Education, National Taichung University of Science and Technology, Taichung 403, Taiwan

⁷ Department of Science Education and Application, National Taichung University of Education, Taichung 403, Taiwan

* Correspondence: cslu6@nutc.edu.tw (C.-S.L.); ccchen@mail.ntcu.edu.tw (C.-C.C.);
Tel.: +886-4-2219-6902 (C.-S.L.); +886-4-2218-3406 (C.-C.C.)

Received: 22 June 2020; Accepted: 29 July 2020; Published: 1 August 2020



Abstract: This study describes the synthesis and characterization of Pt-doped AgInS₂ nanoparticles and reports their prospective application as visible-light catalysts for photodegradation of frequently used pirimicarb insecticides, which pose serious health and environmental concerns. The nanomaterials were characterized by XRD, SEM, TEM, XPS, photoluminescence (PL), and UV–vis diffuse reflectance spectra (DRS). The presented photocatalytic method for water treatment from pirimicarb has the advantages of using visible light source without any costly additive such as H₂O₂ needed in other employed methods. The Pt-doped AgInS₂ exhibited higher photocatalytic activities for pirimicarb degradation than undoped AgInS₂. The 1.0 wt% Pt/AgInS₂ photocatalyst exhibited the highest photodegradation rate, showing enhancement of 56% in comparison to the pure AgInS₂ photocatalyst. The photodegradation rate was found to increase with increasing the catalyst dosage until reaching the optimal dosage of 1.0 g L⁻¹. The pirimicarb degradation was significantly more efficient under acidic conditions, and the rates drastically dropped upon increasing the pH. The photocatalytic mechanism of Pt/AgInS₂ composites and the main active species involved in the process were investigated. The mechanism of pirimicarb degradation was proposed via two different pathways, N-dealkylation and decarbonylation. Lastly, the photocatalysts demonstrated remarkable stability and were reusable in three successive catalytic tests without compromising catalytic activities. The Pt/AgInS₂ photocatalyst also exhibited efficiency and feasibility in pirimicarb removal from environmental lake and river water samples.

Keywords: platinum; AgInS₂; doping; photocatalysis; pirimicarb; water treatment

1. Introduction

Carbamates continue to pose environmental threats as one of the major pesticide families used worldwide, owing to their various efficient biological activities as insecticides, fungicides,

and molluscicides [1]. The main concern with carbamates is their long-term persistence in the environment, with some compounds even remaining for many years after their use. In addition, these compounds are highly soluble in water, which generally leads to unavoidable distribution of their residues by leaching and runoff from soil into both ground and surface water [2]. These residues are found to be increasing in environmental matrices in parallel to the widespread application of carbamates in agriculture. In addition to their environmental effects, carbamates are known to exhibit toxicological effects on human beings, since they are inhibitors of acetylcholinesterase [3]. This family appears on the priority list of the United States Environmental Protection Agency (EPA).

In particular, 2-dimethylamino-5,6-dimethylpyrimidin-4-yl dimethylcarbamate, commonly known as pirimicarb, is one of the frequently applied carbamate derivatives as insecticide for aphids in vegetables and fruits [4]. Pirimicarb is an acetylcholinesterase inhibitor like other carbamate derivatives, and thus it is acutely toxic for mammals. Some studies have reported pirimicarb as a suspected carcinogen and mutagen [5,6]. For example, Soloneski and Larramendy [7] demonstrated the genotoxicity and cytotoxicity of this insecticide in Chinese hamster ovary (CHO-K1) cells. The World Health Organization (WHO) classifies pirimicarb as class II (moderately hazardous). Finding simple and efficient methodologies for pirimicarb removal represents a strongly needed research area especially due to the regular detection of this hazardous compound in environmental waters because of its extensive usage [8,9].

Photocatalysis is currently investigated in wastewater treatment extensively. Photocatalytic methods are promising alternatives that can overcome the current limitations of classical wastewater treatment techniques such as chemical oxidation, activated carbon adsorption, or biological treatments. The prospect of photocatalytic methods is their ability and efficiency in complete degradation of pollutants into harmless products at ambient temperature and pressure [10–12]. Chemical oxidation, for instance, cannot mineralize all organic substances. Adsorption methods involve a phase transfer of pollutants only, i.e., without degradation. Biological treatments are kinetically slow and necessitate the disposal of activated sludge [13,14].

The interest of our group in developing new prospective photocatalytic methods for removal/treatment of contaminants from environmental water continues. Our group has recently demonstrated an efficient UV-driven photodegradation method of pirimicarb using ZnMoO_4 and peroxymonosulfate (PMS). In the tested ZnMoO_4 /PMS/UV system, PMS acted as an acceptor of the photogenerated electrons and generated $\text{SO}_4^{\bullet-}$ radicals upon activation, which led to accelerated photocatalytic degradation of the pollutant [15]. ZnMoO_4 demonstrated stability, reusability, and photocatalytic efficiency in pirimicarb removal from water in the presence of PMS. However, the band gap of ZnMoO_4 is determined to be around 3.01 eV, which rendered this material to be reactive only under UV light irradiation, limiting its solar energy applications. Our group has also reported an efficient pirimicarb degradation method using monoclinic BiVO_4 photocatalysts under visible-light irradiation [16]. Despite the high stability and efficiency of BiVO_4 for pirimicarb removal, the photocatalytic process was dependent on hydrogen peroxide additive to generate significant amount of hydroxyl radical active species [17]. Many studies have previously evaluated the technical and economical practicality of treatment methodologies based on the involved factors such as the need of additives. In essence, the use of H_2O_2 additive is considered to be expensive, and thus it limits the application of BiVO_4 in large-scale treatments of water-soluble pesticides [18]. The main objective of the present study was to examine and reveal a suitable photocatalyst for efficient photodegradation of pirimicarb under visible-light irradiation only, without requiring any other additive such as H_2O_2 . This objective is demonstrated by Table 1 that summarizes the main developed photocatalytic methods for pirimicarb removal in comparison to the reported method herein.

Table 1. Comparison of photocatalytic activity of some photocatalysts with the present photocatalyst for the degradation of pirimicarb.

Photocatalysts	Oxidants	Degradation Efficiency (%)	Degradation Time	Light Source	References
TiO ₂	No oxidant	50%	72 h	UV light	[19]
Single-walled carbon nanotubes-TiO ₂ hybrid	No oxidant	32–33%	30 min	UV light (full light)	[20]
ZnMoO ₄	No oxidant	93%	12 h	UV light	[15]
	PMS	98%	3 h	UV light	[15]
BiVO ₄	No oxidant	<5%	16 h	Visible light	[16]
	H ₂ O ₂	97.6%	4 h	Visible light	[16]
Pt/AgInS ₂	No oxidant	98%	24 h	Visible light	Present work

The synthesis and application of ternary semiconductor nanomaterials with a general formula of XY_mZ_n ($X = \text{Ag, Cu, Cd, Zn}$; $Y = \text{In, Ga}$; $Z = \text{S, Se, Te}$; $m, n = \text{integer}$) has gained more attention in recent years [21,22]. These semiconductors have been found to exhibit excellent optical and electrical characteristics, which led to their diverse efficient applications in optoelectronic devices, linear and nonlinear optical instruments, photovoltaic solar cells, and photocatalysis [23]. Silver indium sulfide (AgInS₂) is highly stable and non-toxic material with remarkable photocatalytic activity towards degradation of organic pollutants, so it is one of the most prospective materials of ternary chalcogenides for these applications [24]. Depending on the crystal structure of AgInS₂, the theoretical band gap of these materials varies between 1.7 and 2.0 eV. Such a band gap is smaller than that of common photocatalysts, such as TiO₂ (3.2 eV), ZnO (3.4 eV), and ZnS (3.6 eV), and is convenient for absorption of visible solar light [25,26]. Li et al. reported the synthesis of AgInS₂ nanoparticles using the microwave hydrothermal method and the photocatalytic efficiency of the prepared materials in dye degradation [27]. However, the photocatalytic activity of a single semiconductor can be limited by the fast recombination of its photogenerated electrons and holes [28]. Noble metal doping is used as an effective modification method to further improve the activity of semiconductor photocatalysts. Noble metal nanoparticle dopants on oxide materials can act as a sink for electrons and can promote interfacial electron transfer due to the high Schottky barriers at the metal—Semiconductor interface [29]. The group of Aazam has investigated Pt-doped AgInS₂ nanoparticles in the photooxidation of cyanide using visible light [30]. The Pt dopant was found to enhance the photocatalytic activity of AgInS₂ significantly. Nevertheless, there has been no detailed study on the photocatalytic mechanism of Pt/AgInS₂ composites and the main active species involved in the process. Furthermore, to the best of our knowledge, the visible-light driven degradation of the commonly used carbamate insecticides in water using Pt/AgInS₂ has not been explored yet.

The present work firstly reports efficient visible-light driven photocatalytic degradation of pirimicarb using Pt-doped AgInS₂ and the systematic studies of optimization of the process via different operational variables (e.g., Pt content, catalytic dosage, and initial pH value). Next, this paper addresses various scavenger investigations and ESR measurements that reveal mechanistic insights of the photocatalytic process underlying high performance of these doped materials and the contribution of major reactive species ($\bullet\text{O}_2^-$, $\bullet\text{OH}$, h^+) in this mechanism. The last section of the report examines the efficiency, stability, and recyclability of the Pt/AgInS₂ photocatalyst in practical treatment of environmental water.

2. Results and Discussion

2.1. Characterization of the As-Prepared Undoped and Pt-Doped AgInS₂ Samples

Figure 1 presents the XRD patterns of undoped and Pt-doped AgInS₂ samples. The patterns infer that the positions of all the diffraction peaks are in agreement with the orthorhombic AgInS₂ phase (JCPDS No. 25-1328). The principal peaks at 2θ of 24.98°, 26.54°, 28.42°, 36.80°, 44.54°, 48.04°,

and 52.62° correspond to the (1 2 0), (0 0 2), (1 2 1), (1 2 2), (3 2 0), (1 2 3), and (3 2 2) planes of orthorhombic-type structure of AgInS_2 , respectively [31]. The same structural characteristics were observed for Pt/AgInS_2 , i.e., orthorhombic AgInS_2 phase as in the pure material, suggesting that platinum doping did not alter the structure of AgInS_2 . No additional diffraction peaks were observed that can be attributed to the presence of the metallic Pt in the Pt/AgInS_2 samples, which is most likely due to the low Pt doping content [30].

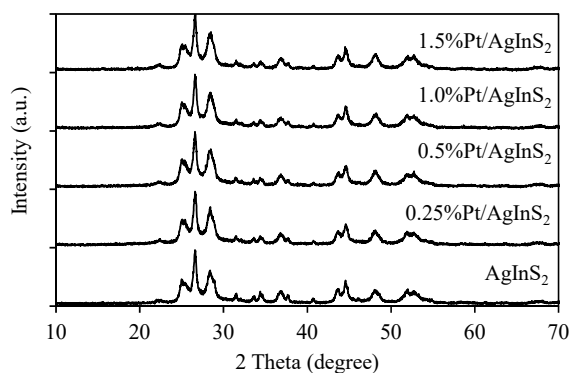


Figure 1. XRD patterns of AgInS_2 and Pt/AgInS_2 photocatalysts.

Next, the samples were characterized using scanning electron microscopy (SEM); a representative micrograph of 1.0 wt% Pt/AgInS_2 sample is displayed in Figure 2a. The SEM micrograph infers that the as-prepared Pt/AgInS_2 product is mainly composed of agglomerated nanoparticles with diameters in the 20–80 nm range. The presence of Pt in these composite materials was confirmed by high-resolution transmission electron microscopy (HRTEM). The HRTEM image of 1.0 wt% Pt/AgInS_2 is presented in Figure 2b. We can observe the AgInS_2 phase with d spacing of 0.31 nm due to (1 2 1) and the Pt phase with d spacing of 0.22 nm due to (1 1 1) are in close contact with each other [31,32].

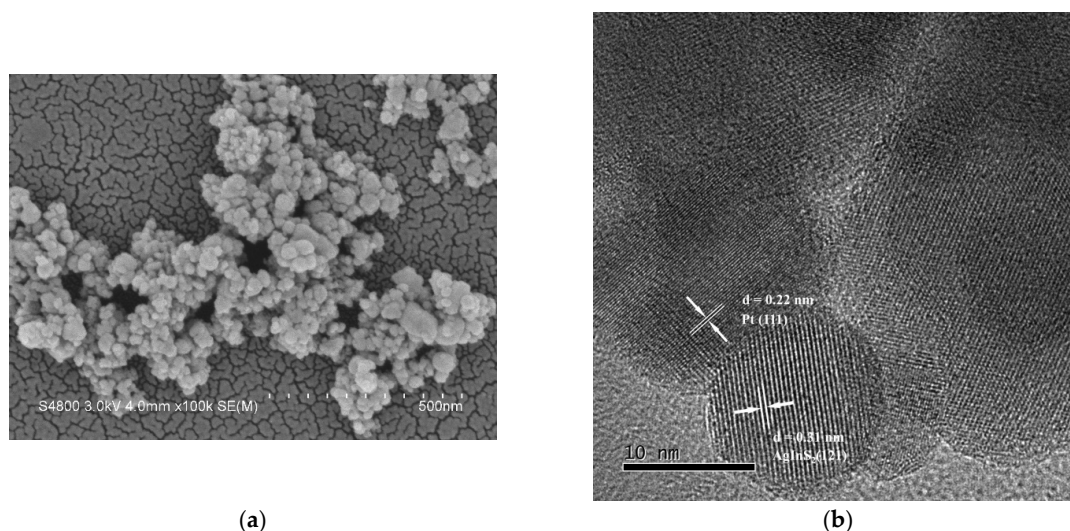


Figure 2. (a) SEM image and (b) TEM image of 1.0 wt% Pt/AgInS_2 photocatalyst.

Figure 3 displays the UV–vis diffuse reflectance spectra of the AgInS_2 and Pt/AgInS_2 samples. A strong absorption in the visible region was observed for all samples, showing a steep absorption edge around 600–700 nm. This shape inferred that the visible-light absorption band was due to the band gap transition and not due to the transition from impurity levels [27]. In order to estimate the band gap energies, the following equation is used: $(\alpha h\nu)^n = k(h\nu - E_g)$, where α is the absorption coefficient, $h\nu$ is the photonic energy, k is a constant, E_g is the absorption band gap energy, and lastly n

is $\frac{1}{2}$ and 2 for an indirect and direct band gaps, respectively [33]. The band gap values were found to be around 1.70~1.72 eV, with insignificant difference among the various prepared samples.

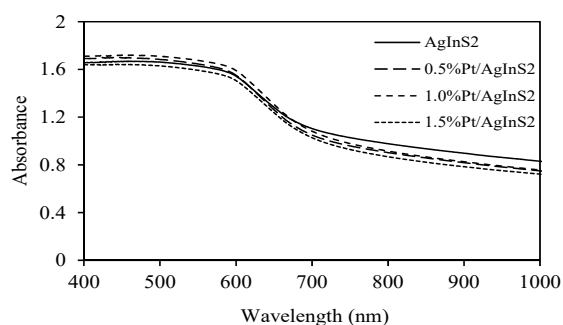


Figure 3. UV-vis diffuse reflectance spectra of AgInS₂ and Pt/AgInS₂ photocatalysts.

XPS analyses were performed to verify the surface chemical composition and the valence state of elements of the Pt/AgInS₂ powder (Figure 4). The spectra of the Ag species (Figure 4a) manifested two symmetric peaks at binding energies of 367.4 and 373.4 eV with a separation of 6 eV, conforming to Ag⁺ ion. They are attributed to the spin-orbit splitting characteristic of Ag 3d_{5/2} and Ag 3d_{3/2}, respectively. The peaks in Figure 4b were observed at about 444.4 and 452.0 eV which are the characteristic of In 3d_{5/2} and In 3d_{3/2}, respectively, corresponding to the presence of indium as In³⁺ [34]. The S 2p spectrum in Figure 4c displayed a strong XPS peak at 161.4 eV, indicating the presence of S²⁻ species in the AgInS₂. The XPS analyses corroborate the XRD results and affirm the composition of the AgInS₂ material. Considering the presence of the Pt dopant in the synthesized materials, Figure 4d shows the XPS for Pt 4f with peaks located at 70.8 and 74.0 eV, corresponding to the binding energies of Pt 4f_{7/2} and Pt 4f_{5/2} [35]. It has been reported that Pt⁰ exhibits Pt 4f_{7/2} and Pt 4f_{5/2} bands in the ranges of 70.2–71.0 and 73.6–74.0 eV, respectively [36]. The XPS result indicated that the oxidation state of Pt on Pt/AgInS₂ is Pt⁰.

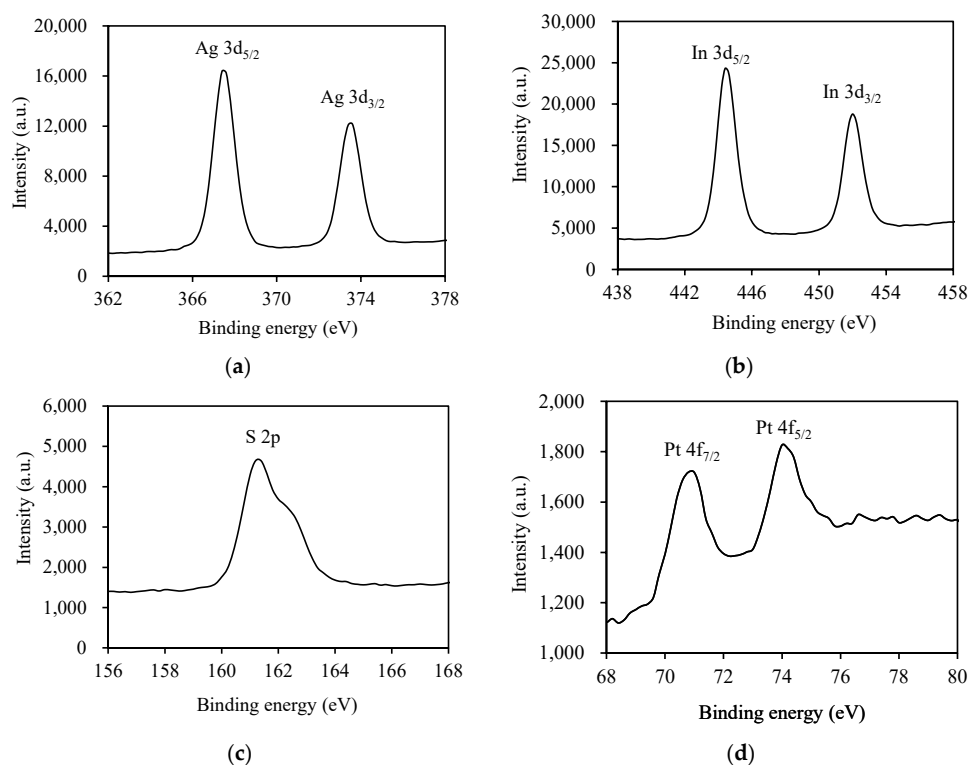


Figure 4. High resolution XPS spectra of 1.0 wt% Pt/AgInS₂ photocatalyst: (a) Ag 3d; (b) In 3d; (c) S 2p; (d) Pt 4f.

Since photoluminescence (PL) emission arises from the recombination of the photogenerated free carriers, PL emission spectroscopy is commonly employed in the investigations of the transfer, separation, and recombination patterns of photogenerated electrons and holes [37]. Figure 5 shows the PL spectra of the pure AgInS_2 and Pt-doped AgInS_2 samples. The PL spectra of Pt-doped AgInS_2 samples showed a significant decrease in intensity in comparison to that of pure AgInS_2 . This weaker intensity indicates a lower recombination probability of free charge carriers. Thus, PL data infer that the Pt doping can effectively inhibit the recombination of photogenerated charge carriers, which helps in separating photogenerated electron-hole pairs in AgInS_2 . However, it can be observed that at higher Pt content, the peak intensity of 1.5 wt% Pt/ AgInS_2 is higher than that of 1.0 wt% Pt/ AgInS_2 . This might be due to the behavior of the Pt dopant as a recombination center conversely when its percentage is high [29].

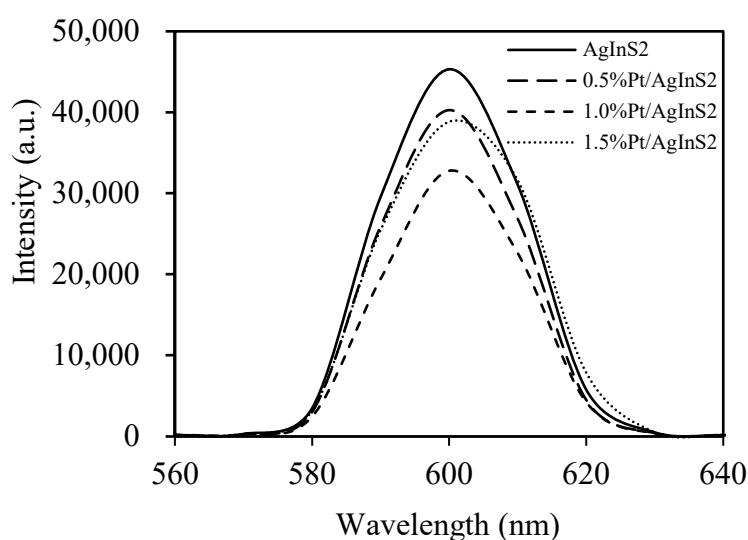


Figure 5. Photoluminescence (PL) emission spectra of AgInS_2 and Pt/ AgInS_2 photocatalysts.

2.2. Photocatalytic Reaction

2.2.1. Effect of Pt Content

Four sets of experiments (adsorptions, photolysis, and photocatalysis) were carried out to verify the role of Pt/ AgInS_2 in the reported reaction. The experiments and relevant results are summarized in Table 2 and Figure 6. In summary, both adsorption experiments (dark conditions, no visible light source) showed an insignificant decrease of pirimicarb (less than 15%), implying that the hydrolysis and adsorption of pirimicarb on AgInS_2 and Pt-doped AgInS_2 was insignificant. Likewise, photolysis showed negligible pirimicarb degradation. On the other hand, the photocatalytic experiments exhibited efficient pirimicarb degradation in aqueous Pt/ AgInS_2 dispersions by visible-light irradiation. ca. 85% of pirimicarb was degraded after irradiation for 24 h.

Table 2. Comparison of pirimicarb degradation between control conditions (catalyst only and visible light only) and photocatalytic conditions.

Experiment	Conditions	Results (After 24 h)
I-Adsorption (no Pt)	◆ Pirimicarb (10 mg L^{-1}) ◆ AgInS ₂ (0.5 g L^{-1}) (No Pt doping, no visible light)	Less than 15% of pirimicarb adsorption
II-Adsorption (Pt)	◆ Pirimicarb (10 mg L^{-1}) ◆ Pt/AgInS ₂ (0.5 g L^{-1}) (No visible light)	Less than 15% of pirimicarb adsorption
III-Photolysis	◆ Pirimicarb (10 mg L^{-1}) ◆ Visible light (No Pt/AgInS ₂)	negligible pirimicarb degradation
IV-Photocatalysis	◆ Pirimicarb (10 mg L^{-1}) ◆ Pt/AgInS ₂ (0.5 g L^{-1}) (Visible light)	85% pirimicarb degradation

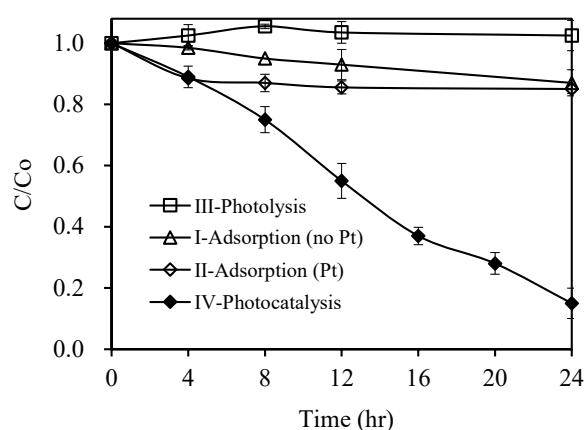
**Figure 6.** Pirimicarb degradation under control conditions (Pt/AgInS₂ only and visible light only) and photocatalytic conditions (experimental conditions: pirimicarb = 10 mg L^{-1} , Pt/AgInS₂ = 0 g L^{-1} in photolysis, 0.5 g L^{-1} in photocatalysis, visible light 1420 lux in photolysis and photocatalysis conditions). Error bars represent the standard deviations of duplicate runs.

Figure 7 presents the influence of the Pt content on the photodegradation rate of pirimicarb under visible-light irradiation. As can be seen, the photocatalytic activity of the Pt-doped AgInS₂ material was significantly higher than that of the undoped AgInS₂. When subjected to visible-light irradiation for 28 h, 93% of pirimicarb degraded in the presence of 1.0 wt% Pt-doped AgInS₂, whereas only 37% of pirimicarb degraded in the presence of undoped AgInS₂. In addition, the degradation rate enhanced from 73% to 93% with increasing the Pt doping content from 0.25 to 1.0 wt%, respectively. The enhanced photocatalytic activities can be rationalized by the improvement of charge separation as a result of the Pt doping. However, the further increase of Pt content (above 1.0 wt%) resulted in a decrease of the photocatalytic activity of the Pt-doped AgInS₂. This result might be explained by the higher recombination of charge carriers as higher Pt doping conversely behave as recombinant centers [29]. These results are in line with the previously discussed effect of Pt doping on the separation of photoinduced electrons and holes in AgInS₂ photocatalysts observed in the PL spectra (Figure 5). In addition, a higher content of Pt might act as a shield that prevents the incident photons from reaching the surface of the catalyst, thereby reducing the photocatalytic activity of the semiconductors [38].

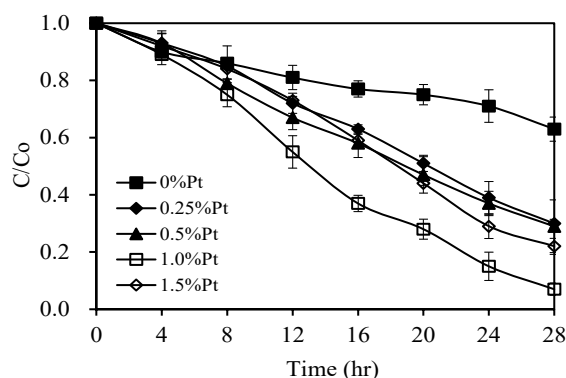


Figure 7. Photocatalytic activities of Pt/AgInS₂ catalysts with different Pt contents. Experimental conditions: pirimicarb concentration 10 mg L⁻¹; photocatalyst concentration 0.5 g L⁻¹; pH 5. Error bars represent the standard deviations of duplicate runs.

Further analysis of the photocatalytic performance of the different materials was performed using regression analysis based on first-order reaction kinetics for the pirimicarb degradation. Degradation rate constants (k_{app}) were calculated from the slope of $\ln C_0/C = k_{app}t$ plots. The k_{app} values as well as the linear regression coefficients for the different studied materials are listed in Table 3. The appropriate first-order relationship shows to fit well, according the obtained values. As shown in Table 3, 1.0 wt% Pt-doping produces the most effective photocatalytic activity for all the AgInS₂ samples. Therefore, the 1.0 wt% Pt-doping samples were chosen as the research object for the subsequent investigations.

Table 3. Kinetic parameters (rate constants and linear regression coefficients R²) for photocatalytic degradation of pirimicarb at various Pt contents.

Pt content (wt%)	k_{app} (hr ⁻¹)	R ²
0	0.015	0.97
0.25	0.043	0.96
0.5	0.045	0.98
1.0	0.092	0.93
1.5	0.055	0.94

2.2.2. Effect of Catalyst Dosage

The amount of the photocatalyst (catalyst dosage) is a parameter that has important effects on photodegradation rates of organic compounds [39,40]. This parameter was examined by using different concentrations of 1.0 wt% Pt/AgInS₂ (0.1 to 1.5 g L⁻¹) in the pirimicarb degradation. The results are shown in Figure 8. In the absence of the catalyst, the degradation of pirimicarb was negligible up to 24 h under visible-light irradiation. The result highlighted the important role of the Pt/AgInS₂ in this application. Figure 8 further displays that the increase in Pt/AgInS₂ concentration from 0.1 to 1.0 g L⁻¹ led to a substantial enhancement of the photodegradation efficiency from 27–98% under visible-light irradiation for 24 h. The optimal catalyst dosage was found to be 1.0 g L⁻¹, after which the degradation rate begins to be in equilibrium. The enhanced photodegradation rates with the increase of the Pt/AgInS₂ dosage can be attributed to the increase in the total surface area (accessible active sites) available for the photocatalytic reaction [41]. Upon catalyst overdose, scattering of incident light and less penetration might occur, causing a loading of 1.5 g/L to have similar degradation rate of pirimicarb as 1.0 g/L.

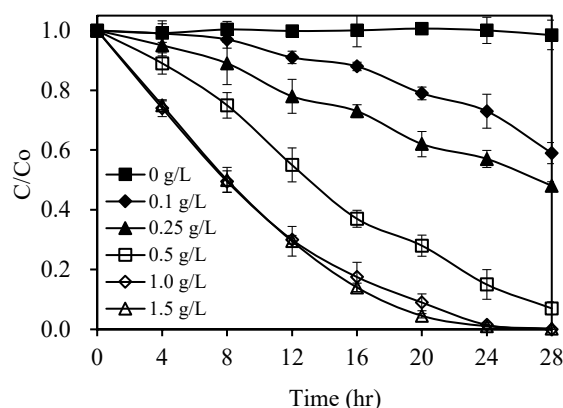


Figure 8. Effect of catalyst dosage on the photocatalytic degradation rate of pirimicarb. Experimental conditions: pirimicarb concentration 10 mg L^{-1} ; pH 5. Error bars represent the standard deviations of duplicate runs.

2.2.3. Effect of Initial Ph Value

The initial pH value of the reaction mixture has been revealed in previous research as an important process parameter with prominent impact on photocatalytic performance [42]. Figure 9 displays the pH effect on pirimicarb photodegradation. The degradation process proceeded significantly faster under an acidic pH, and the degradation rate decreased with the increase of the initial pH. As the pH was increased from 3 to 9, the degradation rate of pirimicarb within 24 h significantly decreased from 98% to 49%. The lower degradation rate at higher pH could be due to a Nernstian shift of the band edges to more negative values, which led to reduction in the oxidation potential of the positive holes [39]. Higher pH and the presence of increased number of hydroxyl groups on the surface might also decrease the conduction band electrons due to electron–hole recombination at active sites [43], which might be another plausible explanation for this observation. In line, Cunningham et al. postulated a model for faster hole–electron recombination at a pH of 9.5, compared to that at lower pH, based on the larger surface concentration of hydroxyls at pH 9.5 [44].

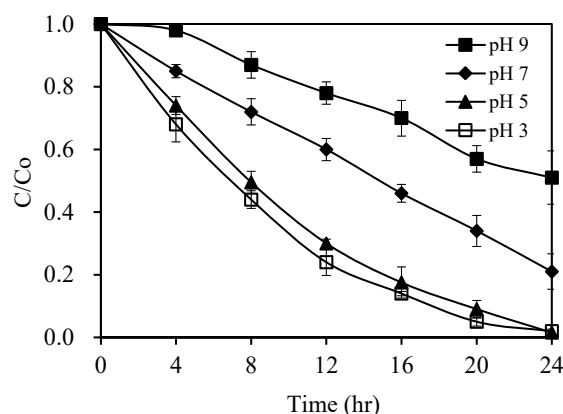


Figure 9. pH effect on the photocatalytic degradation rate of pirimicarb. Experimental conditions: pirimicarb concentration 10 mg L^{-1} ; $1.0 \text{ wt\% Pt/AgInS}_2$ concentration 1.0 g L^{-1} . Error bars represent the standard deviations of duplicate runs.

2.2.4. Identification of Active Species (Quenching and ESR Studies)

The role of potential active species in this photocatalytic process was investigated by adding different scavengers, particularly isopropanol (IPA) for $\bullet\text{OH}$, ethylenediaminetetraacetic acid (EDTA) for h^+ , and benzoquinone (BQ) for $\bullet\text{O}_2^-$ [45]. Figure 10 summarizes the photocatalytic degradation of pirimicarb with $1.0 \text{ wt\% Pt/AgInS}_2$ catalyst under visible-light irradiation in the absence and presence

of each scavenger. In the absence of any scavenger, the photodegradation of pirimicarb was 98% after 24 h of treatment. A dominant inhibition effect on the photodegradation rate (98% to 16%) was observed upon adding IPA (1 mM) to the reaction mixture, evidencing the important role of the $\bullet\text{OH}$ in this reaction. Similar inhibition effect from 98% to 27% was observed upon adding BQ (1 mM), which infers that $\bullet\text{O}_2^-$ also played a role in the photodegradation. In contrast, the addition of EDTA (1 mM) slightly reduced the degradation rate indicating that photogenerated holes played an assistant role in this catalytic degradation of pirimicarb.

Electron spin resonance (ESR) spin-trap technique (with 5,5-dimethylpyridine-*N*-oxide (DMPO)) was employed to further assess and detect the reactive radical species involved in the reactions. Figure 11 displays the results of these experiments. In the absence of light, no ESR signal was observed. Under visible-light irradiation, the characteristic signals for DMPO- $\bullet\text{O}_2^-$ (intensity ratios of 1:1:1:1) and DMPO- $\bullet\text{OH}$ (intensity ratios of 1:2:2:1) spin adducts were observed, indicating the activation of the photocatalysts upon exposure to visible light and the generation of reactive oxygen species such as hydroxyl radical and superoxide anion radical. These results are in line with the generation of $\bullet\text{OH}$ and $\bullet\text{O}_2^-$ radicals under these photocatalytic conditions concluded from the radical scavenger experiments.

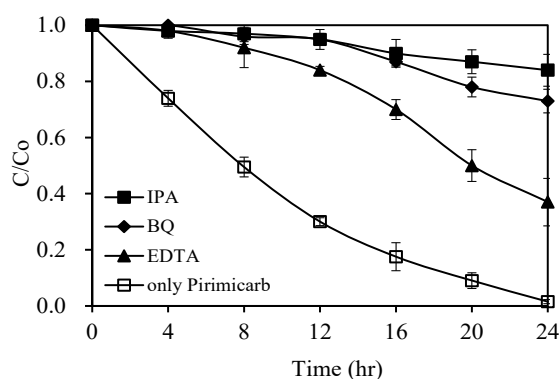


Figure 10. Photocatalytic degradation of pirimicarb with 1.0 wt% Pt/AgInS₂ photocatalyst in the absence and presence of scavengers (isopropanol (IPA), ethylenediaminetetraacetic acid (EDTA), and benzoquinone (BQ)) under visible-light irradiation. Experimental conditions: pirimicarb concentration 10 mg L⁻¹; 1.0 wt% Pt/AgInS₂ concentration 1.0 g L⁻¹; scavenger concentration 1 × 10⁻³ M; pH 5. Error bars represent the standard deviations of duplicate runs.

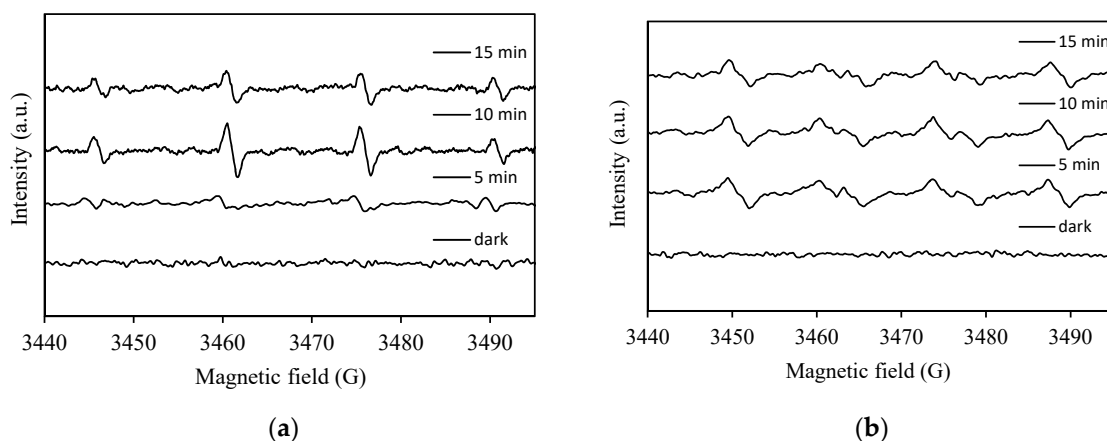


Figure 11. 5,5-dimethylpyridine-*N*-oxide (DMPO) spin-trapping ESR spectra for DMPO- $\bullet\text{OH}$ and DMPO- $\bullet\text{O}_2^-$ under visible-light irradiation with 1.0 wt% Pt/AgInS₂ photocatalyst. (a) DMPO- $\bullet\text{OH}$ (b) DMPO- $\bullet\text{O}_2^-$.

The photocatalytic mechanism of the Pt/AgInS₂ catalysts may be summarized as such: electrons (e⁻) in the valence band (VB) of AgInS₂ are excited to its conduction band (CB) upon irradiation

with visible light creating the same number of holes (h^+) in the VB. In pure $AgInS_2$, the excited charge carriers (electron and hole) rapidly recombine at and/or within the surface of $AgInS_2$ particles, thereby resulting in reduced photocatalytic activity. In contrast, the Pt doped on $AgInS_2$ is believed to serve as an electron sink (Schottky barrier electron trapping) and thus to retard fast charge-pair recombination [46]. In essence, the photoexcited electrons would migrate from the low work function $AgInS_2$ (-4.72 eV) to the high work function noble metal Pt (-5.65 eV) [47,48]. Thus, the incorporated Pt nanoparticles would effectively withdraw electrons from the $AgInS_2$, behaving as efficient electron sinks. Afterwards, Pt can release the accumulated electrons in the presence of efficient acceptors as O_2 forming $\bullet O_2^-$ active radical species which can subsequently form the $\bullet OH$ species [49]. The generated active oxygen species or the oxidative holes in turn attack the organic contaminants and gradually degrade them. Figure 12 summarizes the schematic representation of pirimicarb photodegradation mechanism at the surface of Pt/ $AgInS_2$ catalysts under visible-light irradiation.

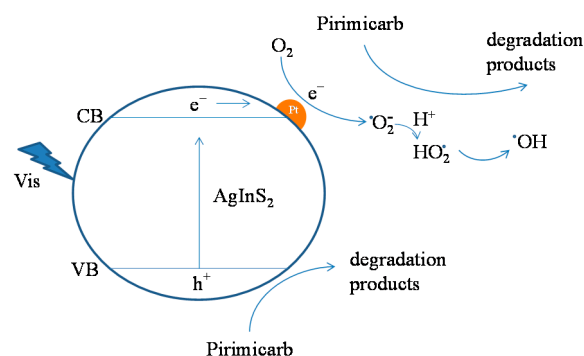


Figure 12. Schematic illustration of the photocatalytic mechanism of the Pt/ $AgInS_2$ photocatalyst.

2.2.5. Reaction Pathway of Pirimicarb Degradation

The analysis of intermediate products was carried out in order to further understand the photodegradation pathway of pirimicarb using Pt/ $AgInS_2$. The chromatogram of the pirimicarb solution after treatment with Pt/ $AgInS_2$ under visible-light irradiation for 16 h is shown in Figure 13. The last peak at 34.11 min represents the pirimicarb (PMC) reactant. Peaks A–G label the main intermediates in the photodegradation process since their intensities increase then subsequently decrease (Figure S1). The summary of the detected chemical entities in this process, their characteristic ions of mass spectra, as well as retention times is depicted in Table 4. The presence of many pirimicarb degradation products can be attributed to the lack of selectivity of the active radical species ($\bullet OH$ and $\bullet O_2^-$) that may attack pirimicarb or the subsequent intermediates at different reactive sites.

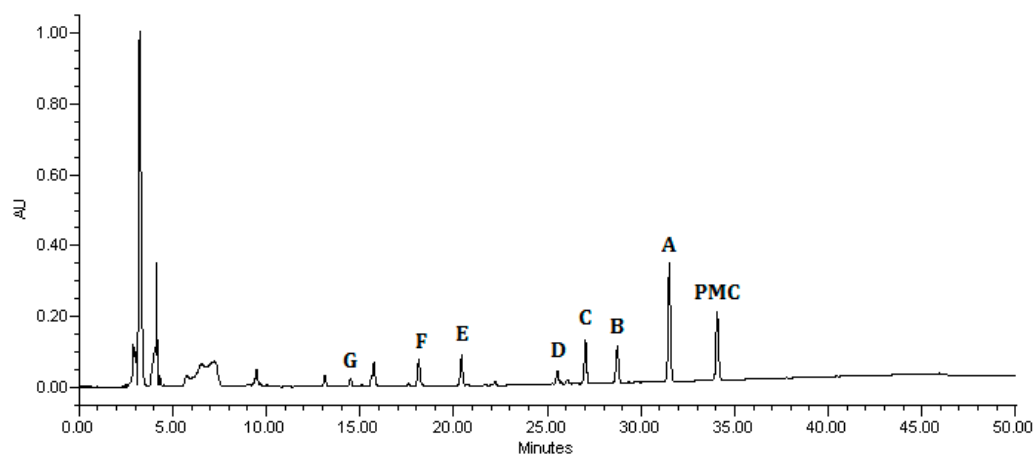
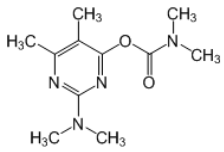
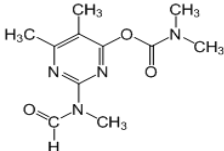
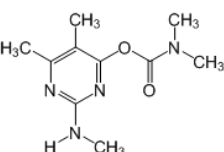
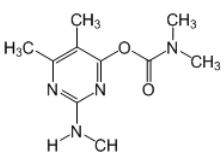
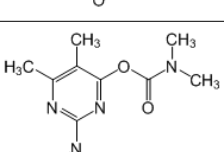
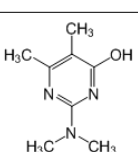
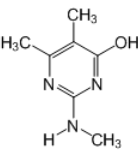
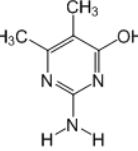


Figure 13. HPLC chromatogram obtained for pirimicarb solution (10 mg L^{-1}) after 16 h of irradiation with visible light in the presence of 1.0 wt% Pt/ $AgInS_2$ catalyst (1.0 g L^{-1}).

The tentative degradation pathway of pirimicarb with two possible routes (**I** and **II**) is suggested in Figure 14 based on our results. Route **I** involves the formation of carbamate intermediates **A–D** via subsequent *N*-dealkylations of the 2-dimethylamine group. The $\bullet\text{OH}$ radicals act on the adjacent C-H bonds to nitrogen, with pronounced stereoelectronic effect that improves the rate of abstraction of H atoms, forming carbon-centered radicals. Furthermore, $\bullet\text{OH}$ radicals can react with the lone-pair electron of the N atom leading to cationic radicals that transform to these carbon-centered radicals [50]. Peroxyl radicals are then formed by oxygen addition to the generated radicals, which in turn decompose to different intermediates (**A** and **B**). Compound **B** can be subject to a second round of successive steps by Pt/AgInS₂ photocatalysis (i.e., H-atom abstraction and oxygen attack), forming the *N*-formyl intermediate **C** and the bi-de-methylated intermediate **D**. Route **II** involves decarbamylation of the carbamate group, which is the second reactive site on pirimicarb, to form the hydroxypyrimidine intermediates **E–G**. 2-dimethylamino-5, 6-dimethyl-4-hydroxypyrimidine (compound **E**) can be formed by pirimicarb decarbamylation via cleavage of its carbonyl–oxygen bond. Compound **F** can be formed either by *N*-dealkylation of 2-dimethylamine of intermediate **E** or by decarbamylation of intermediate **B**. In line, compound **G** is the result of either subsequent *N*-dealkylation of intermediate **F** or decarbamylation of adduct **D**. The results and proposed pathways using this Pt/AgInS₂ catalytic system are similar to pirimicarb photodegradation routes using BiVO₄ that we have reported previously [16].

Table 4. Identification of the intermediates from the photodegradation of pirimicarb by LC/MS.

Structure	t_R (min)	Characteristic Ions (m/z)
	34.11	$[M]^+ = 239, 195, 182$ (PMC) 2-dimethylamino-5,6-dimethylpyrimidin-4-yl-dimethylcarbamate
	31.61	$[M]^+ = 253, 225, 196$ (A) 2-[(methylformyl)amino]-5,6-dimethylpyrimidin-4-yl-dimethylcarbamate
	28.83	$[M]^+ = 225, 180, 168$ (B) 2-methylamino-5,6-dimethylpyrimidin-4-yl-dimethylcarbamate
	27.13	$[M]^+ = 239, 211, 182$ (C) 2-(formylamino)-5,6-dimethylpyrimidin-4-yl-dimethylcarbamate
	25.63	$[M]^+ = 211, 166, 154$ (D) 2-amino-5,6-dimethylpyrimidin-4-yl-dimethylcarbamate
	20.49	$[M]^+ = 168, 123, 98$ (E) 2-dimethylamino-5,6-dimethyl-4-hydroxypyrimidine
	18.31	$[M]^+ = 154, 137, 98$ (F) 2-methylamino-5,6-dimethyl-4-hydroxypyrimidine
	14.70	$[M]^+ = 140, 123, 98$ (G) 2-amino-5,6-dimethyl-4-hydroxypyrimidine

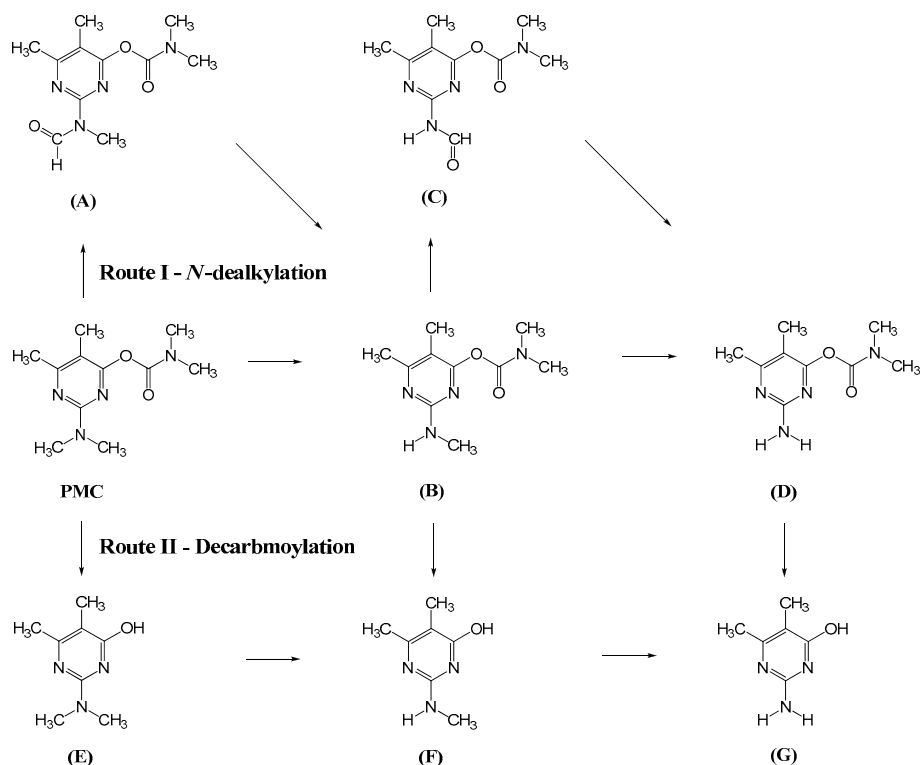


Figure 14. Proposed pirimicarb photodegradation routes after intermediate identifications.

2.2.6. Efficiency of Recycled Catalyst

Practical application of catalysis strongly depends on the reusability and stability of the catalyst materials. For this purpose, the performance of Pt/AgInS₂ materials was studied in three consecutive runs of photodegradation of pirimicarb under visible-light irradiation. The Pt/AgInS₂ catalyst was collected after each run, dried, and reused under the same experimental conditions. As shown in Figure 15a, the photocatalytic activity of Pt/AgInS₂ was consistent after three successive catalytic tests with 98%, 96%, and 92% degradation of pirimicarb, respectively. In addition, Figure 15b displays that the XRD patterns of the used Pt/AgInS₂ powder after the reaction match closely the patterns of the fresh powder before usage, with minor differences in the relative intensities only [31]. The experiments show that the Pt/AgInS₂ system is significantly stable and reusable for long-term practical photocatalytic processes without photocorrosion risk.

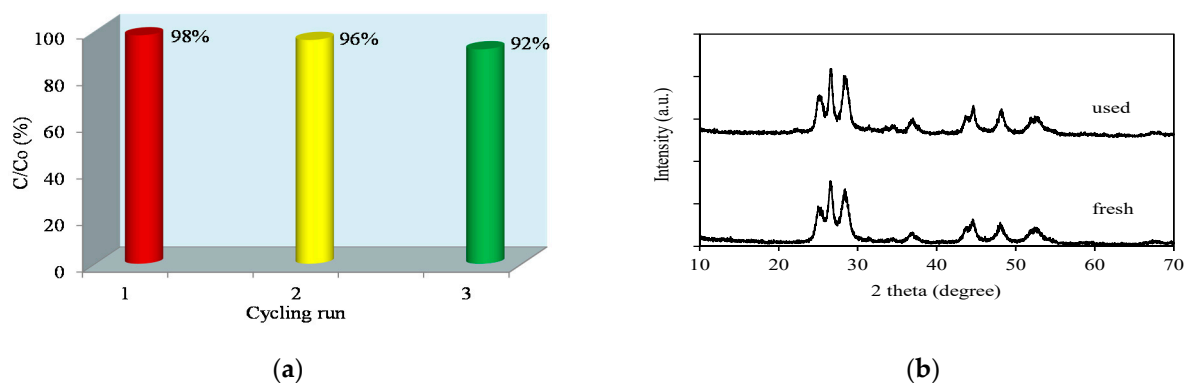


Figure 15. (a) Cycling runs and (b) XRD patterns of 1.0 wt% Pt/AgInS₂ photocatalyst before and after the experiments.

2.2.7. Photocatalytic Treatment of Natural Water Samples

The visible-light driven Pt/AgInS₂ photocatalysis was applied to study the degradation of pirimicarb in the natural water as a reaction medium. The results are summarized in Figure 16 which shows the photodegradation rates of pirimicarb in deionized water and natural water. In the presence of Pt/AgInS₂ photocatalyst, pirimicarb concentration in the natural water samples was found to decrease upon irradiation time. The degradation rate of pirimicarb in natural water samples was slightly reduced in comparison to that in deionized water. This can be due to the presence of organic matter and anions in environmental water (Table 5), which can slightly deactivate the catalyst or compete with the target pirimicarb for the active sites [51]. Despite this slight decrease in rates, the photocatalytic activity of Pt/AgInS₂ in the degradation of pirimicarb is still noticeable even in natural water scenarios, demonstrating the efficiency and prospect of the prepared catalytic system for practical environmental and waste water treatment.

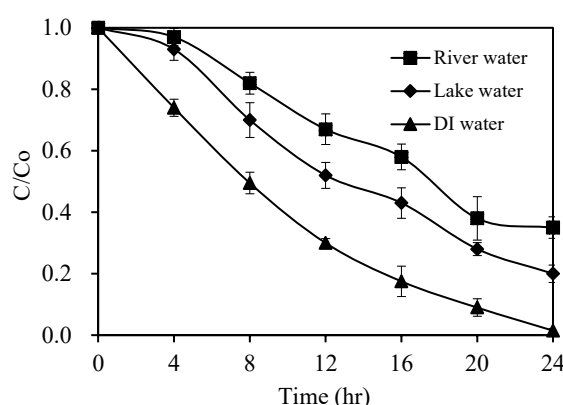


Figure 16. Photocatalytic degradation rates of pirimicarb in deionized water and natural water samples. Experimental conditions: 1.0 wt% Pt/AgInS₂ concentration 1.0 g L⁻¹. Error bars represent the standard deviations of duplicate runs.

Table 5. Characteristics of the real water sample.

Parameter	River Water	Lake Water
pH	6.30	6.24
Conductivity (μmho cm ⁻¹)	420	378
Turbidity (NTU)	2.9	4.9
TOC (mg L ⁻¹)	13.43	3.44
Sulfate (mg L ⁻¹)	48.1	50.9
Chloride (mg L ⁻¹)	22.6	16.7
Nitrate (mg L ⁻¹)	84.8	2.9
Nitrite (mg L ⁻¹)	1.12	0.02

3. Materials and Methods

3.1. Materials

Pirimicarb (99.2%) was purchased from ChemService (West Chester, PA, USA) and employed without any further purification. A stock solution comprising 10 mg L⁻¹ of pirimicarb in water was prepared, protected from light, and stored at 4 °C. The presence of pirimicarb as a pure organic compound was confirmed by HPLC analysis. Silver nitrate AgNO₃ (Aldrich, St. Louis, MO, USA, 99%), indium (III) chloride tetrahydrate (Aldrich, 97%), and L-cysteine (Alfa Aesar, Haverhill, MA, USA 98%) were used as the precursors of silver indium sulfide. Hydrogen hexachloroplatinate (IV) hydrate (Alfa Aesar, 99.9%) was used as source of the Pt dopant. HPLC-grade methanol, nitric acid, sodium hydroxide, and reagent-grade ammonium acetate were obtained from Merck. 5,5-Dimethyl-1-pyrroline-*N*-oxide (DMPO) was purchased from Sigma-Aldrich. Deionized water

was used throughout this study. The water was purified with a Milli-Q water ion-exchange system (Millipore Co. Burlington, MA, USA) for a resistivity of $1.8 \times 10^7 \Omega\text{-cm}$.

3.2. Preparation and Characterization Of Pt/AgInS₂

For the synthesis of AgInS₂ catalyst, 4 mmol of AgNO₃ and 4 mmol of InCl₃·4H₂O were separately dissolved in 20 mL of deionized water each. The AgNO₃ solution was then mixed with the InCl₃·4H₂O solution. A 20 mL of 8 mmol L-cysteine was slowly added to the mixture. The final pH value of the solution was adjusted to 7 using ammonia solution. After stirring for 30 min, the obtained slurry was then transferred into Teflon-lined stainless steel autoclave and heated to 160 °C. After 24 h, the heating was stopped allowing the sample to naturally cool down to room temperature. The obtained precipitate was collected by filtration, washed with absolute ethanol and deionized water several times prior to drying at 60 °C for 12 h. The Pt-doped AgInS₂ catalysts were prepared by the impregnation method using AgInS₂ and hydrogen hexachloroplatinate (IV) hydrate. The as-prepared AgInS₂ powder (0.2 g) was added to 5 mL deionized water containing an appropriate amount of H₂PtCl₆ in a ceramic dish. The suspension was stirred using a glass rod during evaporation of water on the Corning stirrer/plate (Corning, New York, NY, USA). The resulting powder was collected and calcined in an oven at 400 °C for 0.5 h. The content of doping species was calculated according to the mass percentage of Pt. The value for the actual Pt loading of the synthesized catalysts was obtained by using inductively coupled plasma atomic emission spectroscopy (ICP-AES, Optima 2000DV, Wellesley, MA, USA), which is summarized in Table 6.

Table 6. The loading amount of Pt in the catalysts.

Catalysts	Pt Loading (wt%)	
	Intended	Actual
0.25 wt% Pt/AgInS ₂	0.25	0.267
0.5 wt% Pt/AgInS ₂	0.5	0.586
1.0 wt% Pt/AgInS ₂	1.0	1.060
1.5 wt% Pt/AgInS ₂	1.5	1.530

The phase and composition of the as-prepared Pt/AgInS₂ powders were measured using an X-ray diffractometer (PHILIPS X'PERT Pro MPD, Almelo, Netherlands). The morphology of Pt/AgInS₂ powders were analyzed using a field-emission scanning electron microscope (FE-SEM, HITACHI S-4800, Tokyo, Japan). The sample morphology was also observed by a transmission electron microscope (TEM, JEOL JEM-F200, Tokyo, Japan) operated at accelerating voltage of 200 kV. The UV–vis diffuse reflectance spectra of the Pt/AgInS₂ powders were measured using a UV–vis spectrophotometer equipped with an integration sphere (Perkin Elmer Lambda 35, Wellesley, MA, USA). The photoluminescence (PL) emission spectra of Pt/AgInS₂ were obtained using a fluorescence spectrometer (SpectraMax M5, San Jose, CA, USA). The binding energy of Ag, In, S, and Pt was measured at ambient temperature using an X-ray photoelectron spectroscope (XPS, VG Scientific ESCALAB 250, Waltham, MA, USA). The peak position of each element was corrected by C1s (284.6 eV).

3.3. Apparatus and Instruments

The apparatus utilized in the photocatalytic degradation studies of pirimicarb is described elsewhere [52]. The C-75 Chromato-Vue UVP cabinet provided a wide area of illumination from 4 W visible-light tubes positioned on two sides of the cabinet interior. A Waters ZQ LC/MS system, equipped with a binary pump, a photodiode array detector, an autosampler, and a micromass detector, was used for separation and identification. The electron spin resonance (ESR) signals of •OH and •O₂[−] radicals, trapped using 5,5-dimethyl-1-pyrroline-*N*-oxide (DMPO), were recorded using a Bruker EMX A300-10/12 with a microwave bridge (microwave frequency, 9.85 GHz; microwave power, 22.8 mW; modulation amplitude, 1 G; modulation frequency, 100 kHz).

3.4. Procedures and Analyses

Photocatalytic tests were performed on 100 mL of aqueous solutions containing 10 mg L⁻¹ pirimicarb and five different amounts of Pt/AgInS₂ (0.1, 0.25, 0.5, 1.0, and 1.5 g L⁻¹) at different pH values. The initial pH of the suspension in the different tests was adjusted by adding either HNO₃ or NaOH solution. Prior to irradiation, the suspension was magnetically stirred in the dark for ca. 30 min to ensure the establishment of an adsorption/desorption equilibrium. Irradiation was carried out using two fluorescent lamps (F4T5/CW, Philips Lighting Co., Taipei, Taiwan). The lamp mainly provides visible light in the range of 400–700 nm. The average light intensity striking the surface of the reaction solution was about 1420 lux, as measured by a digital luxmeter (XRP-3000 AccuMAX™, Westbury, USA). At any given irradiation time interval, the suspension was sampled (5 mL) and centrifuged (30 min at 3000 rpm) to separate the Pt/AgInS₂ powders. The residual amount of pirimicarb was determined by HPLC after each irradiation cycle. The analysis of organic intermediates was accomplished by high-performance liquid chromatography-electrospray ionization mass spectrometry (HPLC-ESI-MS) after readjusting the chromatographic conditions to make the mobile phase compatible with the working conditions of the mass spectrometer. A 25 mM aqueous ammonium acetate buffer (pH 6.9) was used as solvent A and methanol was used as solvent B. LC was carried out on an Atlantis™ dC₁₈ column (250 mm × 4.6 mm i.d., dp = 5 μm, Milford, USA). The flow rate of the mobile phase was set at 1 mL/min. A linear gradient was run as follows, t = 0, A = 95, B = 5; t = 20, A = 50, B = 50; t = 35–40, A = 10, B = 90; and t = 45, A = 95, B = 5. The elution was monitored at 245 nm. The column effluent was introduced into the ESI source of the mass spectrometer. The quadruple mass spectrometer, equipped with an ESI interface with a heated nebulizer probe at 350 °C, was used with an ion source temperature of 80 °C. ESI was carried out with the vaporizer at 350 °C, and nitrogen was used as sheath (80 psi) and auxiliary (20 psi) gas to assist with the preliminary nebulization and to initiate the ionization process. A discharge current of 5 μA was applied. The tube lens and capillary voltages were optimized for maximum response during the perfusion of the pirimicarb standard.

3.5. Procedure for Degradation of Pirimicarb in Natural Water Samples

The efficiency of the Pt/AgInS₂ photocatalytic system was investigated in natural water samples by collecting river water from the Han River in Taichung City and lake water from the lake in Taichung Park. The suspended solids were removed from all samples by filtration through a 0.45 μm membrane, after which the samples were stored in the dark at 4 °C until analysis. Finally, the natural water samples were spiked with the target compound (at 10 mg L⁻¹) just prior to photocatalytic experiments. Degradations were performed on 100 mL of the natural water samples containing 1.0 wt% Pt/AgInS₂ (1.0 g L⁻¹) without pH adjustment. The photocatalytic activity is expressed by C/C₀ versus t (time), where C is the concentration at a given time and C₀ is the initial concentration of pirimicarb.

4. Conclusions

This work reported that the photocatalytic efficiency of AgInS₂ nanoparticles for pirimicarb degradation could be enhanced considerably upon introducing Pt species. The photocatalytic activity of the Pt/AgInS₂ composite samples improved with increasing Pt content until an optimal loading of 1.0 wt% Pt/AgInS₂, exhibiting the best activity of 98% reduction in pirimicarb concentration after 24 h of visible-light irradiation. The optimal catalytic dosage for this process was found to be 1.0 g L⁻¹. The photodegradation favored under acidic conditions, and the rates decreased with the increase of pH. The main active species in pirimicarb photodegradation were found to be •OH and •O₂⁻ radicals based on scavenger and ESR experiments, while h⁺ showed to play a secondary role in the reaction. Possible routes of the pirimicarb photodegradation were proposed involving dealkylation and decarbonylation pathways. The Pt/AgInS₂ catalytic system demonstrated chemical stability and durable photocatalytic activity in different recycling experiments. The Pt/AgInS₂ photocatalyst was

tested in actual scenarios for pirimicarb degradation in lake and river water samples, revealing its practicality for water treatment.

Supplementary Materials: The following are available online at <http://www.mdpi.com/2073-4344/10/8/857/s1>, Figure S1: Variation in the relative distribution of the intermediate products obtained from the photocatalytic degradation of pirimicarb as a function of irradiation time.

Author Contributions: Conceptualization, C.-S.L., C.-C.C., and H.T.; funding acquisition, C.-S.L.; investigation, H.T., J.S., S.T., V.B.G., S.-Y.W., and Y.-Y.L.; project administration, C.-S.L.; supervision, C.-S.L.; writing—original draft preparation, C.-C.C. and H.T.; writing—review and editing, C.-S.L., J.S., and V.B.G. All authors have read and agreed to the published version of the manuscript.

Funding: This research was funded by the Ministry of Science and Technology of the Republic of China (MOST 108-2113-M-025-001).

Conflicts of Interest: The authors declare no conflict of interest.

References

1. Diuzheva, A.; Dejmikova, H.; Fischer, J.; Andruch, V. Simultaneous determination of three carbamate pesticides using vortex-assisted liquid–liquid microextraction combined with HPLC-amperometric detection. *Microchem. J.* **2019**, *150*, 104071. [[CrossRef](#)]
2. Wu, Q.; Chang, Q.; Wu, C.; Rao, H.; Zeng, X.; Wang, C.; Wang, Z. Ultrasound-assisted surfactant-enhanced emulsification microextraction for the determination of carbamate pesticides in water samples by high performance liquid chromatography. *J. Chromatogr. A* **2010**, *1217*, 1773–1778. [[CrossRef](#)] [[PubMed](#)]
3. Ruengprapavut, S.; Sophonnithiprasert, T.; Pongpoungphet, N. The effectiveness of chemical solutions on the removal of carbaryl residues from cucumber and chili presoaked in carbaryl using the HPLC technique. *Food Chem.* **2020**, *309*, 125659. [[CrossRef](#)] [[PubMed](#)]
4. Chen, T.; Fu, F.; Chen, Z.; Li, D.; Zhang, L.; Chen, G. Study on the photodegradation and microbiological degradation of pirimicarb insecticide by using liquid chromatography coupled with ion-trap mass spectrometry. *J. Chromatogr. A* **2009**, *1216*, 3217–3222. [[CrossRef](#)]
5. Zulfiqar, S.; Rafique, U.; Akhtar, M.J. Removal of pirimicarb from agricultural waste water using cellulose acetate–modified ionic liquid membrane. *Environ. Sci. Pollut. Res.* **2019**, *26*, 15795–15802. [[CrossRef](#)]
6. Champagne, P.-L.; Kumar, R.; Ling, C.-C. Multi-responsive self-assembled pyrene-appended β -cyclodextrin nanoaggregates: Discriminative and selective ratiometric detection of pirimicarb pesticide and trinitroaromatic explosives. *Sens. Actuators B: Chem.* **2019**, *281*, 229–238. [[CrossRef](#)]
7. Soloneski, S.; Larramendy, M.L. Sister chromatid exchanges and chromosomal aberrations in Chinese hamster ovary (CHO-K1) cells treated with the insecticide pirimicarb. *J. Hazard. Mater.* **2010**, *174*, 410–415. [[CrossRef](#)]
8. Fernández-Ramos, C.; Šatínský, D.; Solich, P. New method for the determination of carbamate and pyrethroid insecticides in water samples using on-line SPE fused core column chromatography. *Talanta* **2014**, *129*, 579–585. [[CrossRef](#)]
9. Shi, Z.; Hu, J.; Li, Q.; Zhang, S.; Liang, Y.; Zhang, H. Graphene based solid phase extraction combined with ultra high performance liquid chromatography–tandem mass spectrometry for carbamate pesticides analysis in environmental water samples. *J. Chromatogr. A* **2014**, *1355*, 219–227. [[CrossRef](#)]
10. Omrani, N.; Nezamzadeh-Ejhieh, A. A comprehensive study on the mechanism pathways and scavenging agents in the photocatalytic activity of BiVO₄/WO₃ nano-composite. *J. Water Process. Eng.* **2020**, *33*, 101094. [[CrossRef](#)]
11. Yang, B.; Park, H.-D.; Hong, S.W.; Lee, S.-H.; Park, J.-A.; Choi, J.-W. Photocatalytic degradation of microcystin-LR and anatoxin-a with presence of natural organic matter using UV-light emitting diodes/TiO₂ process. *J. Water Process. Eng.* **2020**, *34*, 101163. [[CrossRef](#)]
12. Chong, M.N.; Jin, B.; Chow, C.; Saint, C.; Saint, C. Recent developments in photocatalytic water treatment technology: A review. *Water Res.* **2010**, *44*, 2997–3027. [[CrossRef](#)] [[PubMed](#)]
13. Wang, K.-H.; Hsieh, Y.-H.; Chou, M.-Y.; Chang, C.-Y. Photocatalytic degradation of 2-chloro and 2-nitrophenol by titanium dioxide suspensions in aqueous solution. *Appl. Catal. B Environ.* **1999**, *21*, 1–8. [[CrossRef](#)]
14. Pelizzetti, E.; Maurino, V.; Minero, C.; Carlin, V.; Tosato, M.L.; Pramauro, E.; Zerbini, O. Photocatalytic degradation of atrazine and other s-triazine herbicides. *Environ. Sci. Technol.* **1990**, *24*, 1559–1565. [[CrossRef](#)]

15. Chen, C.; Fan, H.; Shaya, J.; Chang, Y.; Golovko, V.B.; Toulemonde, O.; Huang, C.; Song, Y.; Lu, C.-S. Accelerated ZnMoO₄ photocatalytic degradation of pirimicarb under UV light mediated by peroxymonosulfate. *Appl. Organomet. Chem.* **2019**, *33*, 5113. [[CrossRef](#)]
16. Wu, Y.; Chen, C.; Huang, Y.; Lin, W.; Yen, Y.; Lu, C. Pirimicarb Degradation by BiVO₄ Photocatalysis: Parameter and Reaction Pathway Investigations. *Sep. Sci. Technol.* **2016**, *51*, 2284–2296. [[CrossRef](#)]
17. Saison, T.; Chemin, N.; Chanéac, C.; Durupthy, O.; Mariey, L.; Maugé, F.; Brezová, V.; Jolivet, J.-P. New Insights Into BiVO₄ Properties as Visible Light Photocatalyst. *J. Phys. Chem. C* **2015**, *119*, 12967–12977. [[CrossRef](#)]
18. Carra, I.; Ortega-Gómez, E.; Santos-Juanes, L.; López, J.L.C.; Sánchez-Pérez, J. Cost analysis of different hydrogen peroxide supply strategies in the solar photo-Fenton process. *Chem. Eng. J.* **2013**, *224*, 75–81. [[CrossRef](#)]
19. Seitz, F.; Bundschuh, M.; Dabrunz, A.; Bandow, N.; Schaumann, G.E.; Schulz, R. Titanium dioxide nanoparticles detoxify pirimicarb under UV irradiation at ambient intensities. *Environ. Toxicol. Chem.* **2012**, *31*, 518–523. [[CrossRef](#)]
20. Dai, K.; Zhang, X.; Fan, K.; Peng, T.; Wei, B. Hydrothermal synthesis of single-walled carbon nanotube–TiO₂ hybrid and its photocatalytic activity. *Appl. Surf. Sci.* **2013**, *270*, 238–244. [[CrossRef](#)]
21. Li, S.; Tang, X.; Zang, Z.; Yao, Y.; Yao, Z.; Zhong, H.; Chen, B. I-III-VI chalcogenide semiconductor nanocrystals: Synthesis, properties, and applications. *Chin. J. Catal.* **2018**, *39*, 590–605. [[CrossRef](#)]
22. Olejniczak, A.; Cichy, B.; Stręk, W. DFT calculations of metal-organic I-III-VI semiconductor clusters: Benchmark of exchange-correlation functionals and localized basis sets. *Comput. Mater. Sci.* **2019**, *163*, 186–195. [[CrossRef](#)]
23. Mousavi-Kamazani, M.; Salavati-Niasari, M. A simple microwave approach for synthesis and characterization of Ag₂S–AgInS₂ nanocomposites. *Compos. Part B Eng.* **2014**, *56*, 490–496. [[CrossRef](#)]
24. Khavar, A.H.C.; Jafarisani, M. Photocatalytic degradation of 4-nitrophenol in aqueous solution by the AgInS₂ nanoparticles synthesized via microwave heating technique. *Int. J. Health Stud.* **2017**, *3*, 18–24.
25. Tang, X.; Choo, E.S.G.; Goh, G.K.L.; Yu, K.; Xu, Q.-H.; Xue, J. Synthesis and characterization of AgInS₂–ZnS heterodimers with tunable photoluminescence. *J. Mater. Chem.* **2011**, *21*, 11239. [[CrossRef](#)]
26. Liu, J.; Chen, S.; Liu, Q.; Zhu, Y.; Lu, Y. Density functional theory study on electronic and photocatalytic properties of orthorhombic AgInS₂. *Comput. Mater. Sci.* **2014**, *91*, 159–164. [[CrossRef](#)]
27. Zhang, W.; Li, D.; Chen, Z.; Sun, M.; Li, W.; Lin, Q.; Fu, X. Microwave hydrothermal synthesis of AgInS₂ with visible light photocatalytic activity. *Mater. Res. Bull.* **2011**, *46*, 975–982. [[CrossRef](#)]
28. Deng, F.; Zhong, F.; Lin, D.; Zhao, L.; Liu, Y.; Huang, J.; Luo, X.; Luo, S.; Dionysiou, D.D. One-step hydrothermal fabrication of visible-light-responsive AgInS₂/SnIn₄S₈ heterojunction for highly-efficient photocatalytic treatment of organic pollutants and real pharmaceutical industry wastewater. *Appl. Catal. B-Environ.* **2017**, *219*, 163–172. [[CrossRef](#)]
29. Ren, J.; Wang, W.; Sun, S.; Zhang, L.; Chang, J. Enhanced photocatalytic activity of Bi₂WO₆ loaded with Ag nanoparticles under visible light irradiation. *Appl. Catal. B Environ.* **2009**, *92*, 50–55. [[CrossRef](#)]
30. Aazam, E. Photocatalytic oxidation of cyanide under visible light by Pt doped AgInS₂ nanoparticles. *J. Ind. Eng. Chem.* **2014**, *20*, 4008–4013. [[CrossRef](#)]
31. Deng, F.; Zhong, F.; Hu, P.; Pei, X.; Luo, X.; Luo, S. Fabrication of In-rich AgInS₂ nanoplates and nanotubes by a facile low-temperature co-precipitation strategy and their excellent visible-light photocatalytic mineralization performance. *J. Nanoparticle Res.* **2017**, *19*, 14. [[CrossRef](#)]
32. Wang, C.; Yin, L.; Zhang, L.; Liu, N.; Lun, N.; Qi, Y. Platinum-Nanoparticle-Modified TiO₂ Nanowires with Enhanced Photocatalytic Property. *ACS Appl. Mater. Interfaces* **2010**, *2*, 3373–3377. [[CrossRef](#)] [[PubMed](#)]
33. Wang, L.; Li, X.; Teng, W.; Zhao, Q.; Shi, Y.; Yue, R.; Chen, Y. Efficient photocatalytic reduction of aqueous Cr(VI) over flower-like SnIn₄S₈ microspheres under visible light illumination. *J. Hazard. Mater.* **2013**, *244*, 681–688. [[CrossRef](#)] [[PubMed](#)]
34. Liu, B.; Li, X.; Zhao, Q.; Ke, J.; Tadé, M.; Liu, S. Preparation of AgInS₂/TiO₂ composites for enhanced photocatalytic degradation of gaseous o-dichlorobenzene under visible light. *Appl. Catal. B-Environ.* **2016**, *185*, 1–10. [[CrossRef](#)]
35. Li, J.; Yue, E.; Lian, L.; Ma, W. Visible light induced dye-sensitized photocatalytic hydrogen production over platinumized TiO₂ derived from decomposition of platinum complex precursor. *Int. J. Hydrogen Energy* **2013**, *38*, 10746–10753. [[CrossRef](#)]

36. Parayil, S.K.; Kibombo, H.S.; Wu, C.-M.; Peng, R.; Kindle, T.; Mishra, S.; Ahrenkiel, S.P.; Baltrusaitis, J.; Dimitrijevic, N.M.; Rajh, T.; et al. Synthesis-Dependent Oxidation State of Platinum on TiO₂ and Their Influences on the Solar Simulated Photocatalytic Hydrogen Production from Water. *J. Phys. Chem. C* **2013**, *117*, 16850–16862. [[CrossRef](#)]
37. Li, F.; Li, X. The enhancement of photodegradation efficiency using Pt–TiO₂ catalyst. *Chemosphere* **2002**, *48*, 1103–1111. [[CrossRef](#)]
38. Qamar, M. Photodegradation of acridine orange catalyzed by nanostructured titanium dioxide modified with platinum and silver metals. *Desalination* **2010**, *254*, 108–113. [[CrossRef](#)]
39. El-Maiss, J.; El Dine, T.M.; Lu, C.-S.; Karamé, I.; Kanj, A.; Polychronopoulou, K.; Shaya, J. Recent Advances in Metal-Catalyzed Alkyl–Boron (C(sp³)-C(sp²)) Suzuki-Miyaura Cross-Couplings. *Catalysts* **2020**, *10*, 296. [[CrossRef](#)]
40. Shaya, J.; Deschamps, M.-A.; Michel, B.Y.; Burger, A. Air-Stable Pd Catalytic Systems for Sequential One-Pot Synthesis of Challenging Unsymmetrical Aminoaromatics. *J. Org. Chem.* **2016**, *81*, 7566–7573. [[CrossRef](#)]
41. Huang, S.; Chen, C.; Tsai, H.; Shaya, J.; Lu, C. Photocatalytic degradation of thiobencarb by a visible light-driven MoS₂ photocatalyst. *Sep. Purif. Technol.* **2018**, *197*, 147–155. [[CrossRef](#)]
42. Lu, C.-S.; Shaya, J.; Fan, H.-J.; Chang, Y.-K.; Chi, H.-T.; Lu, C.-S. Silver vanadium oxide materials: Controlled synthesis by hydrothermal method and efficient photocatalytic degradation of atrazine and CV dye. *Sep. Purif. Technol.* **2018**, *206*, 226–238. [[CrossRef](#)]
43. Annapoorani, R.; Dhananjeyan, M.; Renganathan, R. An investigation on ZnO photocatalysed oxidation of uracil. *J. Photochem. Photobiol. A Chem.* **1997**, *111*, 215–221. [[CrossRef](#)]
44. Cunningham, J.; Corkery, S. Reactions involving electron transfer at semiconductor surfaces. VI. Electron spin resonance studies on dark and illuminated aqueous suspensions of zinc oxides. *J. Phys. Chem.* **1975**, *79*, 933–941. [[CrossRef](#)]
45. Na, Y.; Kim, Y.-I.; Cho, D.W.; Pradhan, D.; Sohn, Y. Adsorption/photocatalytic performances of hierarchical flowerlike BiOBr_xCl_{1-x} nanostructures for methyl orange, Rhodamine B and methylene blue. *Mater. Sci. Semicond. Process.* **2014**, *27*, 181–190. [[CrossRef](#)]
46. Lee, J.; Choi, W. Photocatalytic Reactivity of Surface Platinized TiO₂: Substrate Specificity and the Effect of Pt Oxidation State. *J. Phys. Chem. B* **2005**, *109*, 7399–7406. [[CrossRef](#)]
47. Wang, X.; Waterhouse, G.I.N.; Mitchell, D.R.; Prince, K.; Caruso, R.A. Noble Metal-Modified Porous Titania Networks and their Application as Photocatalysts. *ChemCatChem* **2011**, *3*, 1763–1771. [[CrossRef](#)]
48. Satra, J.; Mondal, P.; Ghorui, U.K.; Adhikary, B. In situ systematic metallic gold incorporation to optimize the photon conversion efficiency of AgInS₂ thin film semiconductor. *Sol. Energy Mater. Sol. Cells* **2019**, *195*, 24–33. [[CrossRef](#)]
49. Ismail, A.A.; Bahnemann, D. One-step synthesis of mesoporous platinum/titania nanocomposites as photocatalyst with enhanced photocatalytic activity for methanol oxidation. *Green Chem.* **2011**, *13*, 428. [[CrossRef](#)]
50. Lee, J.; Choi, W. Effect of Platinum Deposits on TiO₂ on the Anoxic Photocatalytic Degradation Pathways of Alkylamines in Water: Dealkylation and N-Alkylation. *Environ. Sci. Technol.* **2004**, *38*, 4026–4033. [[CrossRef](#)]
51. Xu, X.; Chen, J.; Wang, S.; Ge, J.; Qu, R.; Feng, M.; Sharma, V.K.; Wang, Z. Degradation kinetics and transformation products of chlorophene by aqueous permanganate. *Water Res.* **2018**, *138*, 293–300. [[CrossRef](#)] [[PubMed](#)]
52. Chen, C.C.; Lu, C.S.; Mai, F.D.; Weng, C.S. Photooxidative N-de-ethylation of anionic triarylmethane dye (sulfan blue) in titanium dioxide dispersions under UV irradiation. *J. Hazard. Mater.* **2006**, *137*, 1600–1607. [[CrossRef](#)] [[PubMed](#)]

